

Nanowire Superinductance Fluxonium Qubit

T. M. Hazard,^{1,†} A. Gyenis,^{1,†} A. Di Paolo,^{2,†} A. T. Asfaw,¹ S. A. Lyon,¹ A. Blais,^{2,3} and A. A. Houck^{1,*}

¹*Department of Electrical Engineering, Princeton University, Princeton, New Jersey 08544, USA*

²*Institut quantique and Département de Physique, Université de Sherbrooke, Sherbrooke J1K 2R1 Quebec, Canada*

³*Canadian Institute for Advanced Research, Toronto, M5G 1M1 Ontario, Canada*

 (Received 30 May 2018; revised manuscript received 5 October 2018; published 10 January 2019)

We characterize a fluxonium qubit consisting of a Josephson junction inductively shunted with a NbTiN nanowire superinductance. We explain the measured energy spectrum by means of a multimode theory accounting for the distributed nature of the superinductance and the effect of the circuit nonlinearity to all orders in the Josephson potential. Using multiphoton Raman spectroscopy, we address multiple fluxonium transitions, observe multilevel Autler-Townes splitting and measure an excited state lifetime of $T_1 = 20 \mu\text{s}$. By measuring T_1 at different magnetic flux values, we find a crossover in the lifetime limiting mechanism from capacitive to inductive losses.

DOI: [10.1103/PhysRevLett.122.010504](https://doi.org/10.1103/PhysRevLett.122.010504)

The development of superinductors [1–5] has received significant interest due to their potential to provide noise protection in superconducting qubits [6–8]. Moreover, inductively shunted Josephson junction based superconducting circuits are known to be immune to charge noise [1], and to flux noise in the limit of large inductances [9–12]. Despite remarkable progress, the superinductances that have been so far reported in the literature are still small compared to those needed for qubit protection [7,8,11,12].

A thin-film nanowire built from a disordered superconductor constitutes an alternative approach to reach the required superinductance regime. High-kinetic inductance superconducting materials, such as NbTiN and TiN, have been studied in the context of microwave detectors [13–15], parametric amplifiers [16–18], and rfSQUID qubits [19,20]. In a nanowire, the inertia of the Cooper pair condensate is manifested as the kinetic inductance of the superconducting wire, and can be expressed as

$$L_k = \left(\frac{m}{2e^2 n_s} \right) \left(\frac{l}{wd} \right), \quad (1)$$

where m is the free electron mass, e is the electron charge, and n_s is the density of Cooper pairs [14,21]. The second bracketed term in Eq. (1) is a geometric factor dependent on the length l , width w , and thickness d of the nanowire. By choosing a disordered superconductor with a low n_s and fabricating a sufficiently long and thin wire, the kinetic inductance can be made large enough to reach the superinductance regime. In this regime, the presence of stray ground capacitance and the large kinetic inductance lower the frequencies of the self-resonant modes of the device. As is the case of long junction arrays [2], the multimode structure of the device needs to be taken into account to produce an accurate theoretical description [22,23].

In this Letter, we demonstrate a fluxonium circuit integrating a NbTiN nanowire superinductance. We characterize the effect of the nanowire modes on the qubit spectrum with a multimode circuit theory accounting for the distributed nature of the superinductance. Importantly, and in contrast to previous approaches tailored to weakly anharmonic qubits [24,25], our theory incorporates the circuit nonlinearity to all orders in the Josephson potential. Such difference allows us to treat the strong anharmonicity of the fluxonium qubit efficiently, and to retain the effect of charge dispersion in the multimode Hamiltonian.

A simplified circuit schematic of the nanowire superinductance fluxonium is shown in Fig. 1(a). In contrast to standard fluxonium devices, where a lumped element inductor shunts the Josephson junction [1,3,4,26–28], our circuit model takes into account the fact that the nanowire superinductor is a high-impedance transmission line. We present data from measurements of three devices fabricated on two different films. The nanowires in devices 1 and 2 have widths of 110 and 40 nm, respectively, equal lengths of $730 \mu\text{m}$, and a film thickness of 15 nm. The nanowire in device 3 is fabricated on a 10 nm thick film, has a width of 100 nm, and length of $630 \mu\text{m}$. All the nanowires are fabricated by etching a wire pattern into the NbTiN film, with a single Al/AIO_x/Al junction connecting the two ends of the superinductor together. The qubit on devices 1 and 2 is capacitively coupled to a lumped element Nb resonator, with resonance frequency $\omega_r/2\pi = 6.08 \text{ GHz}$ and a loaded quality factor of $Q = 8,400$. The qubit on device 3 is coupled to a half-wavelength coplanar waveguide resonator with $Q = 14,800$ and $\omega_r/2\pi = 7.50 \text{ GHz}$. An optical image of device 1 is shown in Fig. 1(c).

The fluxonium energy spectrum is obtained by performing two-tone spectroscopy measurements as a function of the external magnetic flux, Φ_{ext} . The amplitude of the

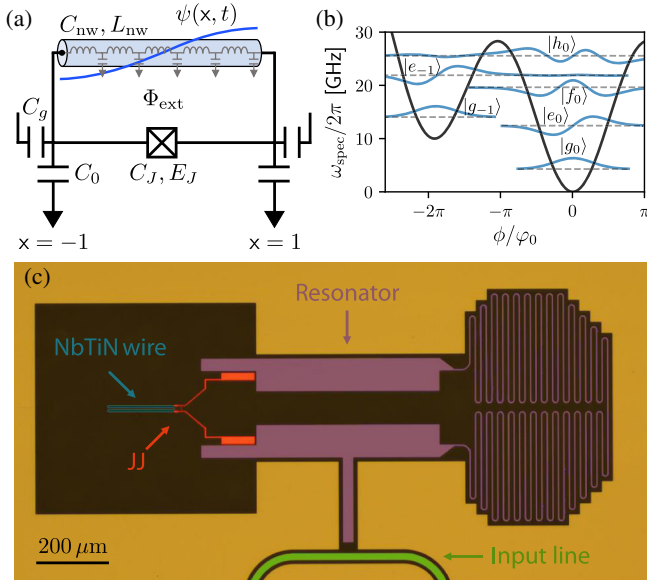


FIG. 1. (a) The circuit diagram for the qubit, with the first antisymmetric standing wave nanowire mode in blue. $\psi(\mathbf{x}, t)$ denotes the flux operator as a function of the dimensionless coordinate $\mathbf{x} = x/l$. An off-chip coil generates the magnetic flux (Φ_{ext}) that is threaded through the loop formed by the nanowire and the junction. C_g and C_0 are the coupling capacitances to the readout resonator and to ground, respectively. (b) The first few fluxonium eigenstates plotted for $\Phi_{\text{ext}}/\varphi_0 = -0.38\pi$, and the respective qubit potential with wells around $\phi/\varphi_0 = -2\pi$ and $\phi/\varphi_0 = 0$, where $\varphi_0 = \hbar/2e$. (c) False colored image of the device with the NbTiN nanowire shown in blue, the single Josephson junction and gate capacitors in red, the readout resonator in purple, and the input transmission line in green.

transmitted power is monitored at the dressed cavity frequency while sweeping a second spectroscopic tone of frequency $\omega_{\text{spec}}/2\pi$. The measurement results are shown in Fig. 2. Labeling the energy eigenstates within a single potential well as $|g_i\rangle, |e_i\rangle, |f_i\rangle, \dots$, where the index i indicates the potential well to which these belong [see Fig. 1(b)], the fluxonium transitions are classified in two types: intrawell plasmons, such as $|g_0\rangle \rightarrow |e_0\rangle$, and interwell fluxons, such as $|g_0\rangle \rightarrow |g_{-1}\rangle$. Parity selection rules of the fluxonium circuit allow for transitions between adjacent plasmon states by absorption of a single photon. However, the direct transition $|g_0\rangle \rightarrow |f_0\rangle$ can only be completed via a two-photon process in which $|e_0\rangle$ serves as an intermediate virtual state. We note that devices 1 and 2 operate in a similar parameter regime to “heavy fluxonium” [9,29], where the ratio between the Josephson (E_J) and charging (E_C) energies is large. As a consequence, transitions between the fluxonium potential wells are exponentially attenuated. Therefore, such excitations are most clearly visible in the regions where they hybridize with the plasmon energy levels.

Figure 2(a) shows the presence of a second fluxonium mode for device 1 at 16.3 GHz. While similar characteristics have been observed in previous fluxonium devices,

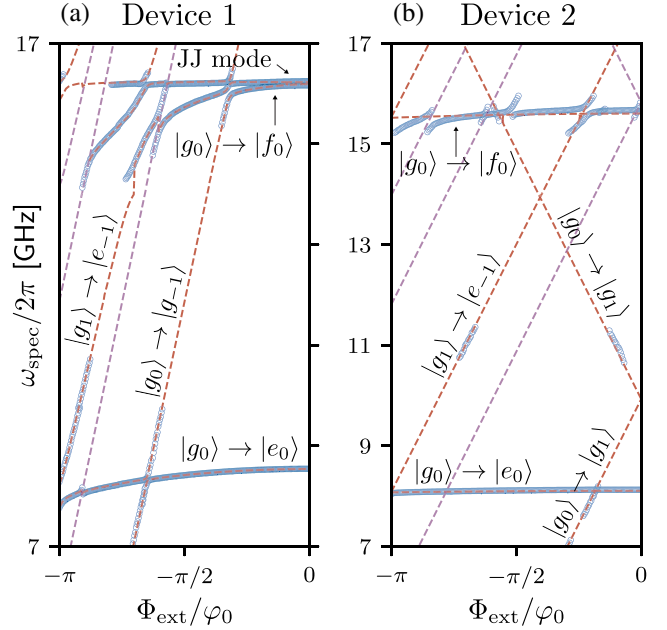


FIG. 2. Two-tone spectroscopy of device 1 (a) and device 2 (b) as a function of Φ_{ext} . The experimentally measured transition frequencies are indicated with blue markers. The result of a fit to the two-mode Hamiltonian in Eq. (5) and detailed in Ref. [30] is shown with red dashed lines corresponding to the fluxonium spectrum and with purple dashed lines indicating sideband transitions [31]. In (a), the inscription “JJ mode” (Josephson junction mode) identifies the second antisymmetric nanowire mode.

high-frequency modes have been so far phenomenologically modeled as harmonic oscillators linearly coupled to the qubit degree of freedom [1]. Here we go beyond such an approximation and derive a multimode Hamiltonian considering the complete device Lagrangian, which accounts for the distributed nature of the superinductance. Importantly, we find that the qubit spectrum is determined by the nonlinear interaction of the circuit modes which are antisymmetric at the Josephson junction ports [see Fig. 1(a)]. The agreement with the measured data is excellent over a very large frequency range.

The nanowire is described as a homogeneous transmission line with distributed capacitance $c = C_{\text{nw}}/2l$ and inductance $\ell = L_{\text{nw}}/2l$, where C_{nw} , L_{nw} , and $2l$ are, respectively, the total ground capacitance, inductance, and length of the nanowire. Defining the flux operator $\psi(\mathbf{x}, t)$ in terms of the dimensionless coordinate $\mathbf{x} = x/l$, the nanowire Lagrangian can be written as

$$\mathcal{L}_{\text{nw}} = \int_{-1}^1 d\mathbf{x} \frac{(C_{\text{nw}}/2)}{2} \dot{\psi}(\mathbf{x}, t)^2 - \frac{1}{2(L_{\text{nw}}/2)} \psi(\mathbf{x}, t)^2. \quad (2)$$

Additionally, we consider gate capacitances (C_g) placed at the two ports of the device ($\mathbf{x}_p = \pm 1$) with respective driving voltages $\{V_{\mathbf{x}_p}\}$, as well as ground capacitances (C_0).

The Lagrangian of the inductively shunted Josephson junction then reads

$$\mathcal{L} = \sum_{\mathbf{x}_p} \frac{C_g}{2} (\dot{\psi}(\mathbf{x}_p, t) - V_{\mathbf{x}_p})^2 + \frac{C_0}{2} \dot{\psi}(\mathbf{x}_p, t)^2 + \mathcal{L}_{\text{nw}} + \frac{C_J}{2} \dot{\delta}_\psi(t)^2 + E_J \cos(\delta_\psi(t)/\varphi_0), \quad (3)$$

where

$$\delta_\psi(t)/\varphi_0 = (\Delta\psi(t) + \Phi_{\text{ext}})/\varphi_0 \quad (4)$$

is the gauge-invariant superconducting phase difference across the junction, $\Delta\psi(t) = \psi(1, t) - \psi(-1, t)$ is the flux operator difference at the boundaries of the superinductor, and E_J is the Josephson energy [32,33].

To obtain a tractable theoretical description of our device, we map Eq. (3) into the Lagrangian of an infinite number of nonlinearly interacting normal modes [30]. We observe that modes which are symmetric at the junction ports are not coupled to the Josephson nonlinearity, and thus do not contribute to the qubit Hamiltonian. We therefore derive a multimode Hamiltonian for the antisymmetric normal modes, which is later truncated to a finite number of modes. The truncation is possible due to the fact that only few antisymmetric modes lie in the frequency range of interest. Furthermore, the effective normal mode impedance decreases quickly with the mode number such that high-frequency modes are only weakly anharmonic.

We find that the spectra of our devices can be accurately described by a two-mode Hamiltonian of the form

$$H_{\text{two-mode}} = \frac{(q_0 - q_{g0})^2}{2\tilde{C}_0} + \frac{\phi_0^2}{2\tilde{L}_0} + \frac{(q_1 - q_{g1})^2}{2\tilde{C}_1} + \frac{\phi_1^2}{2\tilde{L}_1} - \frac{\phi_0\phi_1}{L_J} - E_J \cos\left(\frac{\phi_0 + \phi_1}{\varphi_0} + \frac{\Phi_{\text{ext}}}{\varphi_0}\right), \quad (5)$$

where \tilde{C}_i , \tilde{L}_i , and q_{gi} are, respectively, the effective capacitance, inductance, and offset charge corresponding to the first two antisymmetric modes labeled by $i = \{0, 1\}$ and $L_J = E_J/\varphi_0^2$. The definitions of the various parameters in Eq. (5) is provided in Ref. [30]. The results in Fig. 2 are obtained by numerical diagonalization of the complete Hamiltonian of the device, including Eq. (5), the resonator Hamiltonian, and the interaction between such systems [30].

From our two-mode fit to the qubit spectrum, we find nanowire inductances of 121, 314, and 309 nH for devices 1, 2, and 3, respectively, and corresponding characteristic impedances ($Z_{\text{nw}} = \sqrt{L_{\text{nw}}/C_{\text{nw}}}$) of about 1.85, 7.38, and 12.43 k Ω . The inductance values from the fit are within 7% of the theoretical prediction given by Eq. (1) [30]. Table I provides the Hamiltonian parameters extracted from a single-mode fit allowing direct comparison to

TABLE I. Device parameter table obtained from a single-mode fit to the fluxonium qubit spectrum, for devices 1, 2, and 3.

Device	E_C [GHz]	E_L [GHz]	E_J [GHz]
1	0.89	1.37	10.95
2	0.56	0.52	16.16
3	1.90	0.53	5.90

previous implementations of JJ array based fluxonium devices [1,3,9,10,29].

In devices 1 and 2, the small dipole element between the fluxon states makes it experimentally challenging to directly drive the $|g_{-1}\rangle \rightarrow |g_0\rangle$ transition. By using multiple drives, we are able to transfer the ground state population between the neighboring wells using the intermediate $|h_0\rangle$ state, which is located close to the top of the barrier and has spectral weight in both wells. We apply three coherent and simultaneous drives of frequencies $\omega_\alpha/2\pi$, $\omega_\beta/2\pi$, and $\omega_\gamma/2\pi$, respectively, targeting the $|g_0\rangle \rightarrow |f_0\rangle$ (two-photon), the $|f_0\rangle \rightarrow |h_0\rangle$ (one-photon), and the $|h_0\rangle \rightarrow |e_{-1}\rangle$ (one-photon) transitions [see Fig. 3(a)].

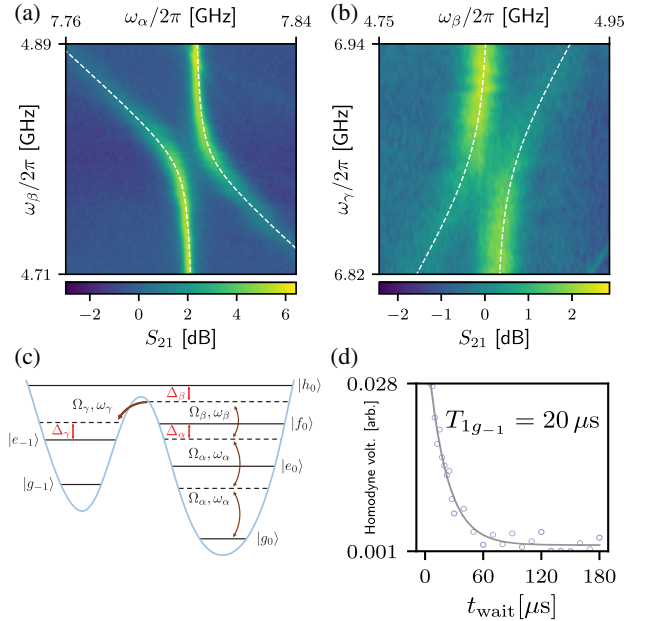


FIG. 3. The multitone spectroscopy data, taken at $\Phi_{\text{ext}}/\varphi_0 = -0.46\pi$, demonstrating population transfer between $|g_0\rangle$ and $|h_0\rangle$ (a) with $\Omega_\gamma = 0$, and $|h_0\rangle$ to $|e_{-1}\rangle$ (b) with fixed $\omega_\alpha/2\pi = 7.78$ GHz. The white dashed lines indicate the maximum population from a multilevel master equation simulation [30]. (c) A schematic diagram of the device 2 level structure in the presence of coherent external drives. The drives, with frequencies $\omega_i/2\pi$ and amplitudes Ω_i are detuned from the levels by $\Delta_i/2\pi$. (d) Three sequential π pulses ($\sigma = 15$ ns) are applied at the transition frequencies to perform T_1 measurements of the $|g_{-1}\rangle$ state. The demodulated homodyne voltage from the readout resonator is measured as a function of t_{wait} .

At $\Phi_{\text{ext}}/\varphi_0 = -0.46\pi$, we set $\Omega_\gamma = 0$ and simultaneously vary $\omega_\alpha/2\pi$ and $\omega_\beta/2\pi$ around the $|g_0\rangle \rightarrow |f_0\rangle$ and $|f_0\rangle \rightarrow |h_0\rangle$ transitions. We observe a vertical band corresponding to the $|g_0\rangle \rightarrow |f_0\rangle$ transition at 7.8 GHz, and a diagonal band with a slope of $\omega_\alpha/\omega_\beta = -1/2$, corresponding to the Raman transition between the $|g_0\rangle$ and $|h_0\rangle$ states [Fig. 3(a)]. Around the resonance condition ($2\hbar\omega_\alpha \approx E_{f_0} - E_{g_0}$ and $\hbar\omega_\beta \approx E_{h_0} - E_{f_0}$), the two bands exhibit an avoided crossing, which is the hallmark of the Autler-Townes doublet previously observed in other superconducting qubits [34–37]. Next, we fix the frequency of the α tone at $\Delta_\alpha/2\pi = 20$ MHz, turn on the γ drive, and simultaneously scan the frequencies $\omega_\beta/2\pi$ and $\omega_\gamma/2\pi$. Figure 3(b) displays the resulting Autler-Townes splitting, where the Raman transition manifests itself here with a slope of $\omega_\gamma/\omega_\beta = +1$, corresponding to the three-drive Raman condition. This method allows us to experimentally determine the energy levels of the fluxonium qubit using population transfer.

With complete information regarding the energy of the fluxonium excited states, we determine the relaxation rate of the $|g_{-1}\rangle$ state by performing time-resolved measurements [38]. We use the frequency values obtained from the Raman spectroscopy and perform a pulse sequence which consists of three sequential π pulses at the transition frequencies $(E_{f_0} - E_{g_0})/h$, $(E_{h_0} - E_{f_0})/h$ and $(E_{h_0} - E_{e_{-1}})/h$ to prepare the system in the $|e_{-1}\rangle$ state. At the end of this procedure, the system relaxes into the $|g_{-1}\rangle$ state, on the timescale of the plasmon T_1 (~ 600 ns). On a longer timescale, the system relaxes back to $|g_0\rangle$. For $t_{\text{wait}} \gg T_{1e_0}$, the reduction in $|g_{-1}\rangle$ population follows an exponential decay with $T_{1g_{-1}} = 20 \mu\text{s}$.

Because of the high E_J/E_C ratio, devices 1 and 2 lack flux insensitive sweet spots at zero and half flux. In order to fully characterize the coherence properties of the qubit and demonstrate coherent control between the fluxon states, we reduced the E_J/E_C ratio in device 3. The overlap between the fluxon wave functions is made sufficiently large to directly observe the transition with a one-photon drive, which comes at the cost of increased sensitivity to different relaxation mechanisms. The low frequency, two-tone spectroscopy data for device 3 are shown in Fig. 4. At $\Phi_{\text{ext}}/\varphi_0 = -\pi$, the spectrum shows a flux-insensitive fluxon transition, where we perform coherence measurements and find $T_1 = 220$ ns, $T_{2\text{Ramsey}} = 380$ ns, and $T_{2\text{Echo}} \approx 2T_1$ indicating that the qubit dephasing is dominated by qubit relaxation.

By changing Φ_{ext} , we measure T_1 of the fluxon transition as a function of qubit frequency. The data show an increase in T_1 as the qubit frequency is increased to a maximal value of $7 \mu\text{s}$ for frequencies between 2–3 GHz. Upon further increasing the qubit frequency, T_1 decreases by an order of magnitude [Fig. 4(c)].

To understand the T_1 frequency dependence, we take into account inductive and capacitive loss mechanisms, which can be described with the following expressions:

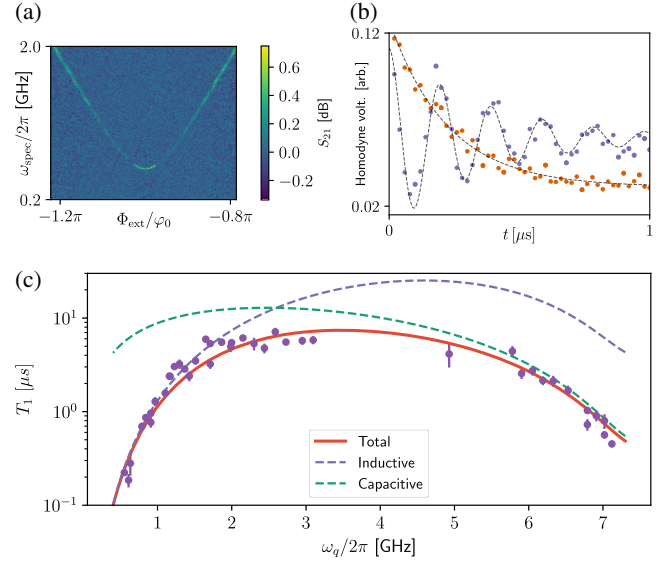


FIG. 4. (a) Low frequency spectroscopy data from device 3. (b) T_1 (red) and $T_{2\text{Ramsey}}$ (blue) data taken at $\Phi_{\text{ext}}/\varphi_0 = -\pi$. (c) T_1 as a function of qubit frequency. The lines represent the theory fits for total (red), inductive (blue), and capacitive (green) T_1 . The T_1 values were obtained with both pulsed and mixed state driving. Measurements using both types of excited state preparation at the same flux gave the same value of T_1 .

$$\Gamma_{\text{ind}} = \frac{E_L}{\hbar Q_L} \left(\coth\left(\frac{\hbar\omega_q}{2k_B T}\right) + 1 \right) |\langle g_{-1} | \hat{\phi} | g_0 \rangle|^2, \quad (6)$$

$$\Gamma_{\text{cap}} = \frac{\hbar\omega_q^2}{8E_C Q_C} \left(\coth\left(\frac{\hbar\omega_q}{2k_B T}\right) + 1 \right) |\langle g_{-1} | \hat{\phi} | g_0 \rangle|^2, \quad (7)$$

where $|\langle g_{-1} | \hat{\phi} | g_0 \rangle|^2$ is the transition matrix element between the fluxon states, Q_L and Q_C are the inductive and capacitive quality factors, respectively, k_B is the Boltzmann constant, T is the temperature, and ω_q is the fluxon transition frequency [39]. Based on previously reported measurements [3], the lifetime limitation from nonequilibrium quasiparticles is at least an order of magnitude larger than the observed relaxation times at all frequencies and is therefore not considered. Radiative loss due to the Purcell effect [40] is only significant when the qubit frequency is within ~ 50 MHz of $\omega_r/2\pi = 7.5$ GHz [30]. Figure 4(c) shows the measured T_1 (blue markers) values along with the fitted $T_1 = (\Gamma_{\text{cap}}^{-1} + \Gamma_{\text{ind}}^{-1})^{-1}$ (red line). The fit of T_1 vs ω_q in Fig. 4, gives $Q_L = 39,000$ and $Q_C = 15,100$, where the lifetime at low ω_q is dominated by inductive loss and at high ω_q by capacitive loss. The inductor can be modeled as a lossless inductor in series with a frequency dependent resistor, where $R = \omega L/Q_{\text{ind}}$ corresponds to $R = 27$ m Ω at $\omega/2\pi = 550$ MHz. The possible sources of the inductive loss can arise from a finite contact resistance between the NbTiN wire and the Al Josephson junction leads, loss from charge impurities on

the surface of the wire, or some intrinsic loss from the bulk NbTiN material. In future devices, the geometry of the Al/NbTiN contact and nanowire dimensions could be modified to better determine what limits the inductive quality factor. Improvements to Q_C could be made by moving to a 3D architecture, where the electric field participation at lossy interfaces is reduced [41].

In conclusion, we have fabricated and measured a nanowire superinductance fluxonium qubit. We find that the transition energy levels are modified due to the distributed nature of the nanowire, which is well explained in the framework of a multimode theory. As the modes of the nanowire strongly depend on the parasitic and stray capacitances of the wire, using a shorter wire with higher sheet inductance (for example high quality granular aluminum films with one hundred times larger $L_k = 2 \text{ nH}/\square$ [42–44]), or integrating the fluxonium into a 3D cavity or waveguide [45], could reduce unwanted capacitances and help to push the nanowire self-resonant modes to higher frequencies. The multimode theory developed here is an important step towards understanding large circuits beyond the lumped element approximation, such as the $0 - \pi$ qubit [7,8], where the distributed nature of the circuit elements is critical to device design.

We thank Andrei Vrajitoarea, Zhaoqi Leng, and Jérôme Bourassa for useful discussions. Research was supported by the Army Research Office Grant No. W911NF-15-1-0421 and the Princeton Center for Complex Materials through the NSF, DMR-1420541. This work was undertaken thanks in part to funding from NSERC and the Canada First Research Excellence Fund.

*corresponding author.

aahouck@princeton.edu

†These authors contributed equally to this work.

- [1] V. E. Manucharyan, J. Koch, L. I. Glazman, and M. H. Devoret, *Science* **326**, 113 (2009).
- [2] N. A. Masluk, I. M. Pop, A. Kamal, Z. K. Mineev, and M. H. Devoret, *Phys. Rev. Lett.* **109**, 137002 (2012).
- [3] I. M. Pop, K. Geerlings, G. Catelani, R. J. Schoelkopf, L. I. Glazman, and M. H. Devoret, *Nature (London)* **508**, 369 (2014).
- [4] U. Vool, I. M. Pop, K. Sliwa, B. Abdo, C. Wang, T. Brecht, Y. Y. Gao, S. Shankar, M. Hatridge, G. Catelani, M. Mirrahimi, L. Frunzio, R. J. Schoelkopf, L. I. Glazman, and M. H. Devoret, *Phys. Rev. Lett.* **113**, 247001 (2014).
- [5] M. T. Bell, I. A. Sadovskyy, L. B. Ioffe, A. Y. Kitaev, and M. E. Gershenson, *Phys. Rev. Lett.* **109**, 137003 (2012).
- [6] L. B. Ioffe, M. V. Feigel'man, A. Ioselevich, D. Ivanov, M. Troyer, and G. Blatter, *Nature (London)* **415**, 503 (2002).
- [7] P. Brooks, A. Kitaev, and J. Preskill, *Phys. Rev. A* **87**, 052306 (2013).
- [8] A. Kitaev, [arXiv:cond-mat/0609441](https://arxiv.org/abs/cond-mat/0609441).
- [9] N. Earnest, S. Chakram, Y. Lu, N. Irons, R. K. Naik, N. Leung, L. Ocola, D. A. Czaplewski, B. Baker, J. Lawrence, J. Koch, and D. I. Schuster, *Phys. Rev. Lett.* **120**, 150504 (2018).
- [10] U. Vool, A. Kou, W. C. Smith, N. E. Frattini, K. Serniak, P. Reinhold, I. M. Pop, S. Shankar, L. Frunzio, S. M. Girvin, and M. H. Devoret, *Phys. Rev. Applied* **9**, 054046 (2018).
- [11] J. M. Dempster, B. Fu, D. G. Ferguson, D. I. Schuster, and J. Koch, *Phys. Rev. B* **90**, 094518 (2014).
- [12] P. Groszkowski, A. D. Paolo, A. L. Grimsmo, A. Blais, D. I. Schuster, A. A. Houck, and J. Koch, *New J. Phys.* **20**, 043053 (2018).
- [13] A. J. Kerman, E. A. Dauler, J. K. W. Yang, K. M. Rosfjord, V. Anant, K. K. Berggren, G. N. Goltsman, and B. M. Voronov, *Appl. Phys. Lett.* **90**, 101110 (2007).
- [14] A. J. Annunziata, D. F. Santavicca, L. Frunzio, G. Catelani, M. J. Rooks, A. Frydman, and D. E. Prober, *Nanotechnology* **21**, 445202 (2010).
- [15] D. F. Santavicca, J. K. Adams, L. E. Grant, A. N. McCaughan, and K. K. Berggren, *J. Appl. Phys.* **119**, 234302 (2016).
- [16] B. Ho Eom, P. K. Day, H. G. LeDuc, and J. Zmuidzinas, *Nat. Phys.* **8**, 623 (2012).
- [17] M. R. Vissers, R. P. Erickson, H.-S. Ku, L. Vale, X. Wu, G. C. Hilton, and D. P. Pappas, *Appl. Phys. Lett.* **108**, 012601 (2016).
- [18] S. Chaudhuri, D. Li, K. D. Irwin, C. Bockstiegel, J. Hubmayr, J. N. Ullom, M. R. Vissers, and J. Gao, *Appl. Phys. Lett.* **110**, 152601 (2017).
- [19] A. J. Kerman, *Phys. Rev. Lett.* **104**, 027002 (2010).
- [20] J. T. Peltonen, P. C. J. J. Coumou, Z. H. Peng, T. M. Klapwijk, J. S. Tsai, and O. V. Astafiev, *Sci. Rep.* **8**, 10033 (2018).
- [21] M. Tinkham, *Introduction to Superconductivity*, 2nd ed. (Dover Publications, Mineola, 2004).
- [22] G. Viola and G. Catelani, *Phys. Rev. B* **92**, 224511 (2015).
- [23] D. G. Ferguson, A. A. Houck, and J. Koch, *Phys. Rev. X* **3**, 011003 (2013).
- [24] S. E. Nigg, H. Paik, B. Vlastakis, G. Kirchmair, S. Shankar, L. Frunzio, M. H. Devoret, R. J. Schoelkopf, and S. M. Girvin, *Phys. Rev. Lett.* **108**, 240502 (2012).
- [25] F. Solgun, D. W. Abraham, and D. P. DiVincenzo, *Phys. Rev. B* **90**, 134504 (2014).
- [26] J. Koch, V. Manucharyan, M. H. Devoret, and L. I. Glazman, *Phys. Rev. Lett.* **103**, 217004 (2009).
- [27] V. E. Manucharyan, N. A. Masluk, A. Kamal, J. Koch, L. I. Glazman, and M. H. Devoret, *Phys. Rev. B* **85**, 024521 (2012).
- [28] G. Zhu, D. G. Ferguson, V. E. Manucharyan, and J. Koch, *Phys. Rev. B* **87**, 024510 (2013).
- [29] Y.-H. Lin, L. B. Nguyen, N. Grabon, J. San Miguel, N. Pankratova, and V. E. Manucharyan, *Phys. Rev. Lett.* **120**, 150503 (2018).
- [30] See Supplemental Material at <http://link.aps.org/supplemental/10.1103/PhysRevLett.122.010504> for detailed information on the multimode Hamiltonian fitting, the multilevel master equation simulation, and sample fabrication.
- [31] A. Wallraff, D. I. Schuster, A. Blais, J. M. Gambetta, J. Schreier, L. Frunzio, M. H. Devoret, S. M. Girvin, and R. J. Schoelkopf, *Phys. Rev. Lett.* **99**, 050501 (2007).
- [32] J. Bourassa, F. Beaudoin, J. M. Gambetta, and A. Blais, *Phys. Rev. A* **86**, 013814 (2012).

- [33] H. L. Mortensen, K. Mølmer, and C. K. Andersen, *Phys. Rev. A* **94**, 053817 (2016).
- [34] M. Baur, S. Filipp, R. Bianchetti, J. M. Fink, M. Göppl, L. Steffen, P. J. Leek, A. Blais, and A. Wallraff, *Phys. Rev. Lett.* **102**, 243602 (2009).
- [35] M. A. Sillanpää, J. Li, K. Cicak, F. Altomare, J. I. Park, R. W. Simmonds, G. S. Paraoanu, and P. J. Hakonen, *Phys. Rev. Lett.* **103**, 193601 (2009).
- [36] S. Novikov, J. E. Robinson, Z. K. Keane, B. Suri, F. C. Wellstood, and B. S. Palmer, *Phys. Rev. B* **88**, 060503 (2013).
- [37] B. Suri, Z. K. Keane, R. Ruskov, L. S. Bishop, C. Tahan, S. Novikov, J. E. Robinson, F. C. Wellstood, and B. S. Palmer, *New J. Phys.* **15**, 125007 (2013).
- [38] M. J. Peterer, S. J. Bader, X. Jin, F. Yan, A. Kamal, T. J. Gudmundsen, P. J. Leek, T. P. Orlando, W. D. Oliver, and S. Gustavsson, *Phys. Rev. Lett.* **114**, 010501 (2015).
- [39] R. J. Schoelkopf, A. A. Clerk, S. M. Girvin, K. W. Lehnert, and M. H. Devoret, [arXiv:cond-mat/0210247](https://arxiv.org/abs/cond-mat/0210247).
- [40] A. A. Houck, J. A. Schreier, B. R. Johnson, J. M. Chow, J. Koch, J. M. Gambetta, D. I. Schuster, L. Frunzio, M. H. Devoret, S. M. Girvin, and R. J. Schoelkopf, *Phys. Rev. Lett.* **101**, 080502 (2008).
- [41] H. Paik, D. I. Schuster, L. S. Bishop, G. Kirchmair, G. Catelani, A. P. Sears, B. R. Johnson, M. J. Reagor, L. Frunzio, L. I. Glazman, S. M. Girvin, M. H. Devoret, and R. J. Schoelkopf, *Phys. Rev. Lett.* **107**, 240501 (2011).
- [42] L. Grünhaupt, N. Maleeva, S. T. Skacel, M. Calvo, F. Levy-Bertrand, A. V. Ustinov, H. Rotzinger, A. Monfardini, G. Catelani, and I. M. Pop, *Phys. Rev. Lett.* **121**, 117001 (2018).
- [43] N. Maleeva, L. Grnhaupt, T. Klein, F. Levy-Bertrand, O. Dupre, M. Calvo, F. Valenti, P. Winkel, F. Friedrich, W. Wernsdorfer, A. V. Ustinov, H. Rotzinger, A. Monfardini, M. V. Fistul, and I. M. Pop, *Nat. Commun.* **9**, 3889 (2018).
- [44] L. Grnhaupt, M. Spiecker, D. Gusenkova, N. Maleeva, S. T. Skacel, I. Takmakov, F. Valenti, P. Winkel, H. Rotzinger, A. V. Ustinov, and I. M. Pop, [arXiv:1809.10646](https://arxiv.org/abs/1809.10646).
- [45] A. Kou, W. C. Smith, U. Vool, R. T. Brierley, H. Meier, L. Frunzio, S. M. Girvin, L. I. Glazman, and M. H. Devoret, *Phys. Rev. X* **7**, 031037 (2017).

I. SUPPLEMENTARY INFORMATION

A. Fabrication details

Device fabrication begins with sputtering 15 nm of NbTiN onto a 500 μm thick C-plane sapphire substrate. A small patch of NbTiN, where the nanowire will be fabricated later in the process, is protected with MicropositTM S1811 photoresist and the remaining NbTiN is removed with an SF₆/Ar dry etch. For the lumped element readout resonator and transmission line, 200 nm of Nb is sputtered over the areas of the chip which had no NbTiN and subsequently patterned and etched with another SF₆/Ar dry etch. Next, a layer of ZEP520A (1:1 dilution in anisole) e-beam resist is spun on the chip and the nanowire pattern is exposed and developed with standard e-beam lithography techniques. Finally, an MMA/PMMA bilayer e-beam resist is placed on the chip and the Josephson junction layer is patterned with e-beam lithography. To ensure metallic contact between the junction and the NbTiN nanowire, a high-voltage Ar ion beam milling process is used to remove the native oxid layer formed on the surface of the NbTiN film. The JJ layer is fabricated with a double angle evaporation of 30 nm and 60 nm of Al, with a 15 minute oxidation step in between the first and second evaporation angles to form the oxide layer of the junction. For measurement, the samples are attached to the base plate of a dilution refrigerator with a mixing chamber temperature of 12 mK.

B. Properties of NbTiN film

Room temperature resistance measurements are performed on 7 different nanowires with $l = 100 \mu\text{m}$ and varying widths, ranging from 50 to 900 nm. From these measurements, we extract a sheet resistivity of $R = 97 \pm 5 \Omega/\square$. Temperature dependent resistivity measurements on the film used in devices 1 and 2 show a superconducting critical temperature of $T_c = 9.5 \text{ K}$. The resistance increases by $\sim 20\%$ as the film is cooled from room temperature to right above T_c . From scanning electron microscope images and the resistance measurements of the test structures, we infer nanowire widths of $110 \pm 5 \text{ nm}$ and $40 \pm 5 \text{ nm}$ for the two devices. Based on the resistivity, T_c , and the geometry of the nanowires, we estimate an $n_s = 7.0 \times 10^{25} \text{ m}^{-3}$. The predicted inductances based on Eq. (1) are $L_k = 112$ and $L_k = 309 \text{ nH}$ for devices 1 and 2, respectively. This is within 7% and 2% of the two-mode fit values in Eq. 5 of the main text. Similar resistance and T_c measurements on the 10 nm thick NbTiN film used for device 3 predict an $L_k = 307 \text{ nH}$, which is $< 1\%$ from the measured value of 308 nH.

C. Modeling of the Autler-Townes splitting

We model the system with a four-level Hamiltonian which, in the $(|g_0\rangle, |f_0\rangle, |h_0\rangle, |e_{-1}\rangle)$ energy eigenbasis and in the absence of external drives, reads

$$H_0 = E_{g_0} |g_0\rangle \langle g_0| + E_{f_0} |f_0\rangle \langle f_0| + E_{h_0} |h_0\rangle \langle h_0| + E_{e_{-1}} |e_{-1}\rangle \langle e_{-1}|, \quad (1)$$

where the groundstate energy is chosen to be $E_{g_0} = 0$, and the energies of excited levels satisfy the relations $E_{g_0} < E_{f_0}$, $E_{e_{-1}} < E_{h_0}$ (see figure 3 (a) of the main text). We work in a semiclassical picture where the external drives $\omega_\alpha/2\pi$, $\omega_\beta/2\pi$, $\omega_\gamma/2\pi$ with respective Rabi frequencies Ω_α , Ω_β , Ω_γ introduce coupling exclusively between neighboring energy levels. In the rotating-wave approximation, this situation is described by the interaction Hamiltonian

$$H_{\text{int}} = \frac{1}{2} \hbar \Omega_\alpha (|f_0\rangle \langle g_0| e^{-i2\omega_\alpha t} + |g_0\rangle \langle f_0| e^{i2\omega_\alpha t}) + \frac{1}{2} \hbar \Omega_\beta (|h_0\rangle \langle f_0| e^{-i\omega_\beta t} + |f_0\rangle \langle h_0| e^{i\omega_\beta t}) + \frac{1}{2} \hbar \Omega_\gamma (|e_{-1}\rangle \langle h_0| e^{i\omega_\gamma t} + |h_0\rangle \langle e_{-1}| e^{-i\omega_\gamma t}). \quad (2)$$

Since $E_{h_0} > E_{e_{-1}}$, the time-dependent phase corresponding to the third term in Eq. (2) has the opposite sign. Combining the above expressions, the total Hamiltonian of the system is defined as $H = H_0 + H_{\text{int}}$

$$H = \begin{bmatrix} 0 & \frac{\hbar\Omega_\alpha}{2}e^{i2\omega_\alpha t} & 0 & 0 \\ \frac{\hbar\Omega_\alpha}{2}e^{-i2\omega_\alpha t} & E_{f_0} & \frac{\hbar\Omega_\beta}{2}e^{i\omega_\beta t} & 0 \\ 0 & \frac{\hbar\Omega_\beta}{2}e^{-i\omega_\beta t} & E_{h_0} & \frac{\hbar\Omega_\gamma}{2}e^{-i\omega_\gamma t} \\ 0 & 0 & \frac{\hbar\Omega_\gamma}{2}e^{i\omega_\gamma t} & E_{e_{-1}} \end{bmatrix}. \quad (3)$$

We now move to the rotating frame of the drives by applying the unitary $U = |g_0\rangle\langle g_0| + e^{i2\omega_\alpha t}|f_0\rangle\langle f_0| + e^{i(2\omega_\alpha+\omega_\beta)t}|h_0\rangle\langle h_0| + e^{i(2\omega_\alpha+\omega_\beta-\omega_\gamma)t}|e_{-1}\rangle\langle e_{-1}|$, which results in

$$\tilde{H} = \begin{bmatrix} 0 & \frac{1}{2}\hbar\Omega_\alpha & 0 & 0 \\ \frac{1}{2}\hbar\Omega_\alpha & \hbar\Delta_\alpha & \frac{1}{2}\hbar\Omega_\beta & 0 \\ 0 & \frac{1}{2}\hbar\Omega_\beta & \hbar(\Delta_\alpha + \Delta_\beta) & \frac{1}{2}\hbar\Omega_\gamma \\ 0 & 0 & \frac{1}{2}\hbar\Omega_\gamma & \hbar(\Delta_\alpha + \Delta_\beta - \Delta_\gamma) \end{bmatrix}. \quad (4)$$

Here, the detunings are $\hbar\Delta_\alpha = E_{f_0} - 2\hbar\omega_\alpha$, $\hbar\Delta_\beta = E_{h_0} - E_{f_0} - \hbar\omega_\beta$ and $\hbar\Delta_\gamma = E_{h_0} - E_{e_{-1}} - \hbar\omega_\gamma$. We account for dissipation in the system with a Lindblad master equation of the form

$$\dot{\rho} = -\frac{i}{\hbar}[H, \rho] + \sum_j \left[c_j \rho c_j^\dagger - \frac{1}{2}\{c_j^\dagger c_j, \rho\} \right], \quad (5)$$

where the collapse operators c_j are defined as $c_j = \sum_i \sqrt{\Gamma_{ij}}\sigma_{ij}$, for given energy states $|i\rangle$ and $|j\rangle$, where Γ_{ij} is the decay rate between them and $\sigma_{ij} = |i\rangle\langle j|$. The steady-state solution of Eq. (5) is numerically obtained and the maximal excited state population, $\max(\rho_{f_0 f_0} + \rho_{h_0 h_0} + \rho_{e_{-1} e_{-1}})$, is shown with dashed lines in figure 3 (b) and (c) of the main text.

D. Pulse calibration for population transfer

The amplitude of the π pulses is found by measuring Rabi-oscillations between consecutive levels in device 2 at $\Phi_{\text{ext}}/\phi_0 = -0.46\pi$. The amplitude of each pulse is chosen based on the value for which the oscillation between adjacent levels reaches its first extrema. First, we determine the amplitude of the $g_0 \rightarrow f_0$ pulse. Second, after applying a π pulse between states g_0 and f_0 , we apply a second pulse of varying amplitude corresponding to the $h_0 \rightarrow f_0$ transition frequency to observe Rabi oscillations between h_0 and f_0 . Finally, we apply these two π pulses ($g_0 \rightarrow f_0$, $f_0 \rightarrow h_0$), and then a third pulse of varying amplitude to perform Rabi oscillation between h_0 and e_{-1} . The measured T_1 of e_{-1} state is ~ 600 ns.

E. Raw Two-tone spectroscopy data

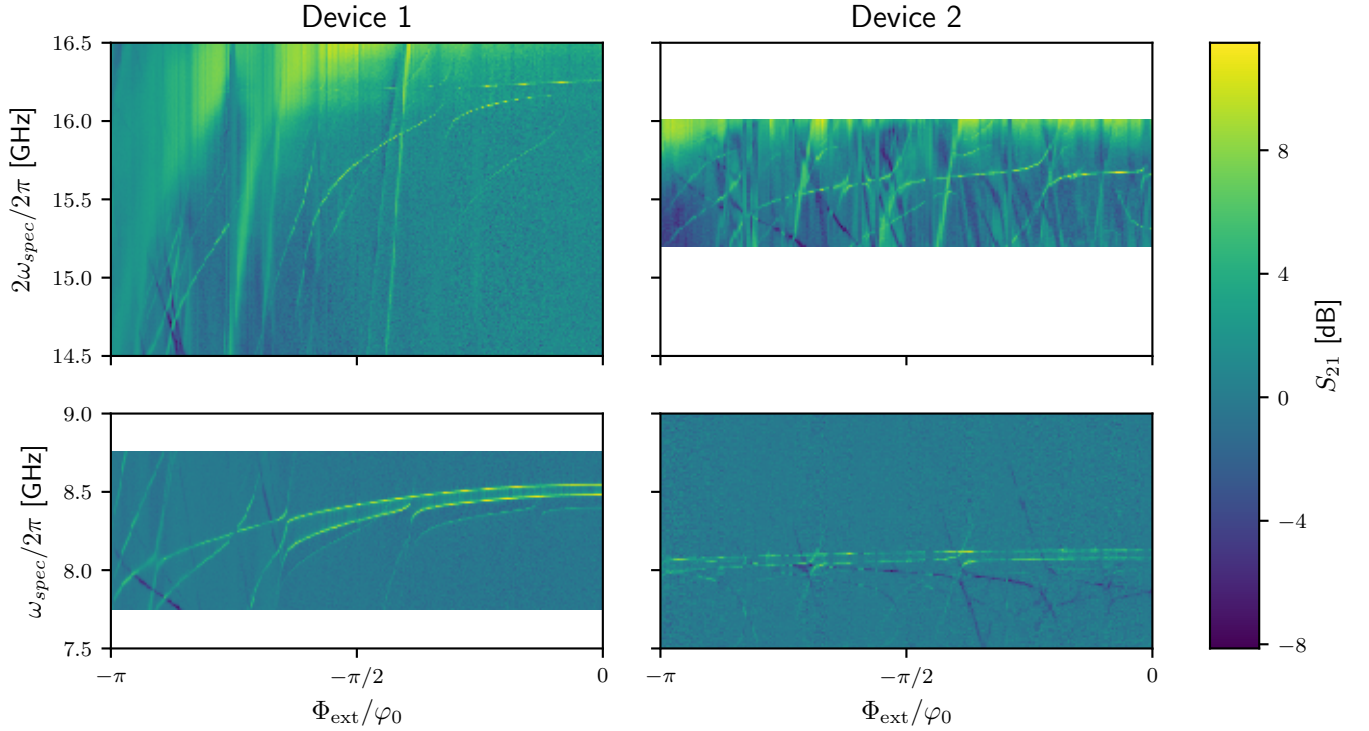


FIG. 1. The amplitude response of the cavity transmission when applying a second spectroscopic tone ($\omega_{\text{spec}}/2\pi$) taken at different Φ_{ext} for devices 1 and 2. The data points in Fig. 2 of the main text were obtained by finding the peak positions of the spectroscopic data. The upper panels correspond to the two-photon peaks and the lower panels correspond to the single photon data. The satellite peaks on the raw data is a result of the presence of thermal cavity photons.

F. Spectrum Characterization

1. Multimode Hamiltonian

In this section, we outline the theory developed to treat the multimode structure of the device in figure 1 (a) of the main text. Our derivation is inspired by ideas introduced in Refs. [1–3]. For simplicity, we assume the absence of disorder in gate and ground capacitances, although the effect of a small amount of disorder is discussed below.

Considering the fluxonium Lagrangian of main text Eq. 3, we first introduce approximations to reduce the problem to that of two nonlinearly interacting bosonic modes, which is then numerically diagonalized to fit the experimentally measured spectrum of Fig. 2 in the main text.

The circuit normal modes are a convenient basis where the fluxonium Hamiltonian is diagonal to second order in the Josephson nonlinearity. In addition, the symmetry of such modes unequivocally identifies the degrees of freedom that are effectively coupled to the JJ. For these modes only does the Josephson non-linearity needs to be taken into account. Writing the wave equation which holds in the bulk of the nanowire $\partial_t^2 \psi(x, t) = \omega_{\text{nw}}^2 \partial_x^2 \psi(x, t)$, with $\omega_{\text{nw}} = 1/\sqrt{(C_{\text{nw}}/2)(L_{\text{nw}}/2)}$, we look for normal modes of the form

$$\psi_m(x, t) = u_m(x)\xi_m(t), \quad (6)$$

satisfying $u_m''(x) = -k_m^2 u_m(x)$ and $\ddot{\xi}_m(t) = -\omega_m^2 \xi_m(t)$. Here, k_m is a dimensionless wave vector and $\omega_m = \omega_{\text{nw}} k_m$ (linear dispersion). The mode frequencies are determined by the boundary conditions that we derive taking the continuous limit of the equations of motion for the discretized field $\psi(x, t) \rightarrow \{\phi(x_n)\}$, where $\phi(x_n)$ is defined in a

lattice with $2N + 1$ points in the range $[-1, 1]$. To this end, we consider the lattice Lagrangian linearized in absence of the external voltage drives and flux ($V_{\pm 1}, \varphi_{\text{ext}} \rightarrow 0$), for which the equations of motion simply read

$$\mathbf{C}\ddot{\boldsymbol{\phi}} + \mathbf{L}^{-1}\boldsymbol{\phi} = \mathbf{0}. \quad (7)$$

Here, \mathbf{C} and \mathbf{L}^{-1} are, respectively, the capacitance and (inverse) inductance matrices for the lattice model, while $\boldsymbol{\phi}$ is the corresponding $2N + 1$ -dimensional node-flux vector. As illustrated in Fig. 2, the transmission line is modeled as a chain of $2N$ LC resonators, with single nodes connected to ground by a capacitance $\Delta x C_{\text{nw}}/2$ and neighboring nodes coupled by an inductance $\Delta x L_{\text{nw}}/2$. Taking the continuous limit of Eq. (7) by letting $\Delta x \rightarrow 0$ and $N \rightarrow \infty$ with $N\Delta x = 1$, we find the field boundary conditions

$$\mathbf{C}_{\text{bc}}\ddot{\boldsymbol{\psi}}_{\text{bc}} + \mathbf{L}_{\text{bc}}^{-1}\boldsymbol{\psi}_{\text{bc}} = \mathbf{0}, \quad (8)$$

where $\boldsymbol{\psi}_{\text{bc}} = (\psi(1, t), \psi(-1, t))^T$, $\mathbf{C}_{\text{bc}} = C_{\Sigma}\mathbb{1} - C_J\sigma_x$ and $\mathbf{L}_{\text{bc}} = \left[\frac{x}{(L_{\text{nw}}/2)}\partial_x + \frac{1}{L_J} \right]\mathbb{1} - \frac{1}{L_J}\sigma_x$. Here, we have defined the identity ($\mathbb{1}$) and Pauli-X (σ_x) matrices, the capacitances $C_{\Sigma} = C_p + C_J$ and $C_p = C_g + C_0$, and the operators (x, ∂_x), which are evaluated at the boundaries $x_p = \pm 1$. We note that our formalism can be also applied to more general superconducting circuits including distributed elements.

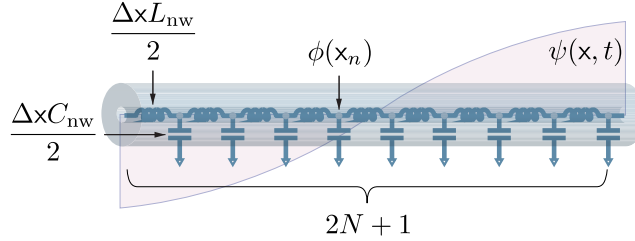


FIG. 2. Discretized model for the nanowire including $2N + 1$ nodes with ground capacitance $\Delta x C_{\text{nw}}/2$ and coupling inductance $\Delta x L_{\text{nw}}/2$. The field operator $\psi(x, t)$ is replaced by the node flux operators $\{\phi(x_n)\}$ defined in the lattice.

We now consider $\psi(x, t)$ to be the normal mode solution in Eq. (6), and parametrize the mode function as

$$u_m(x) = A_m \cos(k_m x) + B_m \sin(k_m x), \quad (9)$$

where A_m, B_m are constants to be determined. With this choice, Eq. (8) can be rewritten in the form $\mathbf{M}(A_m, B_m)^T = \mathbf{0}$, where \mathbf{M} is a coefficient matrix (omitted for brevity). Nontrivial solutions to this homogeneous system of equations follow from the condition $\det(\mathbf{M}) = 0$, implying

$$\frac{C_p}{2} L_{\text{nw}} \omega_m^2 + k_m \tan k_m = 0, \quad (10)$$

or

$$\frac{L_J}{L_{\text{nw}}} k_m + \left[1 - \left(C_J + \frac{C_p}{2} \right) L_J \omega_m^2 \right] \tan k_m = 0. \quad (11)$$

Eq. (10) and Eq. (11) allow us to find the modes frequencies $\{\omega_m\}$, which are then plugged back into Eq. (8) to determine the mode function Eq. (9). We stress that Eq. (10) does not include any of the Josephson junction parameters. In fact, this equation determines the frequency of symmetric nanowire modes, which have zero voltage difference across the Josephson junction: $\Delta u_m = u_m(1) - u_m(-1) = 0$. In contrast, Eq. (11) depends on C_J and L_J , and determines the frequency of antisymmetric modes which do couple to the junction ($\Delta u_m \neq 0$). This fundamental difference is discussed in more detail below.

We are now in position to expand the field in the normal mode basis, as

$$\psi(x, t) = \sum_m u_m(x) \xi_m(t), \quad (12)$$

where, in principle, the sum over m is extended to all circuit modes. Making use of the orthogonality relations [1, 4]

$$\int_{-1}^1 dx (C_{\text{nw}}/2) u_m(x) u_n(x) + C_J \Delta u_m \Delta u_n + \sum_{x_p} C_p u_m(x_p) u_n(x_p) = C_m \delta_{mn}, \quad (13)$$

and

$$\int_{-1}^1 dx \frac{1}{(L_{\text{nw}}/2)} u'_m(x) u'_n(x) + \frac{\Delta u_m \Delta u_n}{L_J} = \frac{\delta_{mn}}{L_m}, \quad (14)$$

where $L_m^{-1} = C_m \omega_m^2$, and substituting Eq. (12) into Eq. 3 of the main text, we arrive to the circuit Lagrangian in the normal mode basis

$$\mathcal{L} = \sum_m \frac{C_m}{2} \dot{\xi}_m^2 + \sum_{x_p} C_g u_m(x_p) V_{x_p} \dot{\xi}_m - \frac{\xi_m^2}{2L_m} + E_J [\cos(\delta_\psi/\varphi_0) + (\Delta\psi/\varphi_0)^2/2], \quad (15)$$

where explicit time dependence has been omitted and δ_ψ/φ_0 is defined in Eq. 4 of the main text. We note that Eq. (15) is diagonal to second order in the Josephson potential for $\Phi_{\text{ext}} = 0$, as a consequence of our normal mode basis choice. Writing

$$\Delta\psi = \sum_m \Delta u_m \xi_m, \quad (16)$$

we verify that symmetric modes do not couple to the Josephson nonlinearity, thus behaving as a collection of non-interacting harmonic oscillators. Accordingly, we disregard symmetric modes in our treatment and consider the set $\{\tilde{m}\}$, consisting of antisymmetric modes for which $\Delta u_{\tilde{m}} \neq 0$. With the change of variables $\phi_{\tilde{m}} = \Delta u_{\tilde{m}} \xi_{\tilde{m}}$, we rewrite Eq. (15) as

$$\mathcal{L} = \sum_{\tilde{m}} \frac{\tilde{C}_{\tilde{m}}}{2} \dot{\phi}_{\tilde{m}}^2 + \sum_{x_p} C_g \frac{u_{\tilde{m}}(x_p)}{\Delta u_{\tilde{m}}} V_{x_p} \dot{\phi}_{\tilde{m}} - \frac{\phi_{\tilde{m}}^2}{2\tilde{L}_{\tilde{m}}} + \sum_{\tilde{m} < \tilde{n}} \frac{1}{L_J} \phi_{\tilde{m}} \phi_{\tilde{n}} + E_J \cos(\delta_\psi/\varphi_0), \quad (17)$$

where δ_ψ/φ_0 conserves the definition in main text Eq. 4 with the replacement $\Delta\psi/\varphi_0 = \sum_{\tilde{m}} \phi_{\tilde{m}}/\varphi_0$. Here,

$$\begin{aligned} \tilde{C}_{\tilde{m}} &= C_{\tilde{m}}/\Delta u_{\tilde{m}}^2, \\ \tilde{L}_{\tilde{m}}^{-1} &= \frac{1}{\Delta u_{\tilde{m}}^2} \int_{-1}^1 dx \frac{u'_{\tilde{m}}(x)^2}{(L_{\text{nw}}/2)}, \end{aligned} \quad (18)$$

denote the mode \tilde{m} effective capacitance and inductance, respectively. The multimode Hamiltonian

$$H = \sum_{\tilde{m}} H_{\tilde{m}}^{(0)} + H_{\text{int}}, \quad (19)$$

follows immediately from Eq. (17), and includes the set of noninteracting terms $\{H_{\tilde{m}}^{(0)}\}$, with

$$H_{\tilde{m}}^{(0)} = \frac{(q_{\tilde{m}} - q_{g\tilde{m}})^2}{2\tilde{C}_{\tilde{m}}} + \frac{\phi_{\tilde{m}}^2}{2\tilde{L}_{\tilde{m}}}, \quad (20)$$

where $q_{g\hat{m}} = \sum_{x_p} C_g u_{\hat{m}}(x_p) V_{x_p} / \Delta u_{\hat{m}}$, and the interaction potential

$$H_{\text{int}} = - \sum_{\hat{m} < \hat{n}} \frac{\phi_{\hat{m}} \phi_{\hat{n}}}{L_J} - E_J \cos \left(\sum_{\hat{m}} \frac{\phi_{\hat{m}}}{\varphi_0} + \frac{\Phi_{\text{ext}}}{\varphi_0} \right). \quad (21)$$

Eq. (19) is approximated into a tractable Hamiltonian making use of a frequency and effective impedance hierarchy of the normal modes. Indeed, if these are sorted in frequency as $\omega_0 < \omega_1 < \dots < \omega_n$, it is possible to see that $Z_0 \gg Z_1 \gg \dots \gg Z_n$. Therefore, as the frequency range of interest is bounded, a good approximation for Eq. (19) can be obtained taking into account a finite number of modes covering such a spectral range, and considering the rest of the modes in a vacuum state. We note that vacuum fluctuations are strongly suppressed for high-frequency modes, thanks to their vanishing effective impedance. In our particular case, the experiment probes frequencies in $[0, \omega_{\text{max}}]$, with $\omega_0 < \omega_{\text{max}} < \omega_1, \omega_{\text{max}} \ll \omega_2$. Therefore, we approximate the device's Hamiltonian by the two-mode Hamiltonian in main text Eq. 5, which includes the two first antisymmetric modes. As shown in Fig. 2 of the main text, we find excellent agreement between the main text Eq. 5 diagonalization and the measured fluxonium spectrum. Moreover, we verify that the inclusion of the third antisymmetric normal mode in the fluxonium Hamiltonian does not modify appreciably the qubit spectrum. Regarding device 1, an estimation of a dispersive-like coupling strength for the first order mode-mode interaction gives $g^2/\Delta < 100$ kHz between the first and third JJ modes, and $g^2/\Delta < 1$ kHz between the second and third JJ modes, while the same quantities are negligible for device 2.

We note that the symmetry of the self-resonant nanowire modes is lost in the presence of circuit disorder. However, if disorder is small ($< 10\%$), one can still work in the symmetric-antisymmetric normal mode basis, deriving a capacitive coupling between the two sets of modes proportional to the amount of disorder. Therefore, the effect of symmetric modes could be taken into account within a dispersive (thus perturbative) theory, as it was previously done in the literature [5, 6]. However, due to the generality of our fit routine (see Sect. IF 2), we do not find necessary to consider such a dispersive shift (which adds a fit parameter) to obtain a high-accuracy agreement between theory and experiment.

Finally, we highlight some important differences of our formalism to previous approaches. We note that the full cosine potential of the Josephson junction has been exactly resummed in Eq. (17), before proceeding to the quantization in Eq. (19). Importantly, this step allows us to treat the strong nonlinearity of the fluxonium qubit efficiently by exact diagonalization of Eq. (19) in the phase basis, and to recover the effect of charge dispersion. Other approaches including Black-Box quantization [7, 8], rely on a series expansion of the cosine potential in terms of bosonic creation and annihilation operators for the normal modes. While this method has been proved to be convenient for the study of weakly anharmonic devices, it is not straightforward to capture the physics of strongly nonlinear devices for which a potentially infinite number of terms in the series expansion of the cosine potential needs to be considered.

The problem of characterizing the multimode structure of the fluxonium qubit has also been addressed for the case of Josephson junction array based devices by considering the normal modes of the superinductor [2, 3]. While this approach was successfully used to understand the overall complexity of these devices and study the effect of the multimode structure on the coherence times of the qubit, it is not of direct applicability to our experimental setup and to our experimental results.

To conclude, we note that our theory admits a purely discrete formulation where the nanowire is modeled as chain of LC oscillators (see Fig. 2) and the normal modes of the fluxonium device are computed by means of Eq. (7). For $N > 100$, the normal mode structure of such a system converges quickly to the result in the continuous limit and reproduces the results in Fig. 2 of the main text.

2. Fluxonium Spectrum

As the two-tone spectroscopy experiment probes the qubit spectrum in presence of the resonator, our data includes the Lamb shift contribution arising as a consequence of the dispersive coupling between the fluxonium and the resonator.

Lamb and dispersive shifts can be computed by means of the bare qubit level structure using the framework developed in [6], for any qubit-resonator system in the dispersive regime. Equivalently, such quantities can be obtained from full diagonalization of the transversally coupled qubit-resonator Hamiltonian. In this work, we use the second approach to compute the qubit spectrum.

We assume a readout resonator of nominal frequency (ω_r) and impedance (Z_r), according to the measured resonator mode frequency and specifications. Considering first, a single mode \hat{m} in Eq. (20), and making use of the antisymmetry of the mode function, the corresponding voltage coupling operator, as derived from the offset charge term, takes the

form $-q_{\dot{m}}(C_g/\tilde{C}_{\dot{m}})(V_1 - V_{-1})/2$. In the present case, the weak fluxonium-resonator coupling Hamiltonian is obtained by replacing the voltage difference ($V_1 - V_{-1}$) by the resonator voltage operator $V_r = \sqrt{\hbar Z_r/2}(a + a^\dagger)$, where a (a^\dagger) is the photon annihilation (creation) operator. Therefore, in a two-mode approximation for the fluxonium qubit, we consider the complete Hamiltonian

$$H = H_r + H_{\text{two-mode}} + H_{r0} + H_{r1}, \quad (22)$$

where $H_r = \omega_r a^\dagger a$ denotes the resonator Hamiltonian, $H_{\text{two-mode}}$ is given in Eq. 5 of the main text, and $H_{r\dot{m}}$

$$H_{r\dot{m}} = -q_{\dot{m}}(C_g/\tilde{C}_{\dot{m}})\sqrt{\hbar Z_r/2}(a + a^\dagger)/2 \quad (23)$$

is the coupling Hamiltonian between the resonator and the \dot{m}^{th} fluxonium mode.

The Lamb-shifted i^{th} qubit energy-level is identified by the energy eigenstate of Eq. (22) exhibiting maximum overlap with $|0, i\rangle$ (0 resonator excitations, i fluxonium excitations). The fluxonium parameters $C_p, C_J, L_J, C_{\text{nw}}, L_{\text{nw}}$, and the fluxonium-resonator coupling capacitance C_c , are considered input variables for the qubit spectrum fit in Fig. 2 of the main text. The results of the fit are listed in Table I.

Device	C_g [fF]	C_p [fF]	C_J [fF]	L_J [nH]	C_{nw} [fF]	L_{nw} [nH]
1	14.33	30.20	3.52	14.33	35.49	121.38
2	15.89	60.89	4.67	9.82	5.79	314.75

TABLE I. Circuit element parameters as obtained from the two-mode fit to the fluxonium qubit spectra presented in Fig. 2 of the main text.

-
- [1] J. Bourassa, F. Beaudoin, J. M. Gambetta, and A. Blais, Phys. Rev. A **86**, 013814 (2012).
 - [2] G. Viola and G. Catelani, Phys. Rev. B **92**, 224511 (2015).
 - [3] D. G. Ferguson, A. A. Houck, and J. Koch, Phys. Rev. X **3**, 011003 (2013).
 - [4] H. L. Mortensen, K. Mølmer, and C. K. Andersen, Phys. Rev. A **94**, 053817 (2016).
 - [5] V. E. Manucharyan, J. Koch, L. I. Glazman, and M. H. Devoret, Science **326**, 113 (2009).
 - [6] G. Zhu, D. G. Ferguson, V. E. Manucharyan, and J. Koch, Phys. Rev. B **87**, 024510 (2013).
 - [7] S. E. Nigg, H. Paik, B. Vlastakis, G. Kirchmair, S. Shankar, L. Frunzio, M. H. Devoret, R. J. Schoelkopf, and S. M. Girvin, Phys. Rev. Lett. **108**, 240502 (2012).
 - [8] F. Solgun, D. W. Abraham, and D. P. DiVincenzo, Phys. Rev. B **90**, 134504 (2014).